The Astrophysical Journal Letters, 988:L25 (10pp), 2025 July 20 https://doi.org/10.3847/2041-8213/adeaac

Impact of Two-population α-particle Distributions on Plasma Stability

Mihailo M. Martinović[1], Kristopher G. Klein[1], Rossana De Marco[2], Daniel Verscharen[3], Roberto Bruno[2], and Raffaella D'Amicis[2]
[1] Lunar and Planetary Laboratory, University of Arizona, Tucson, AZ 85721, USA; mmartinovic@arizona.edu
[2] INAF—Istituto di Astrofisica e Planetologia Spaziali, Via Fosso del Cavaliere 100, 00133 Rome, Italy
[3] Mullard Space Science Laboratory, University College London, Dorking RH5 6NT, UK
Received 2025 January 9; revised 2025 June 24; accepted 2025 July 2; published 2025 July 17

Abstract

The stability of weakly collisional plasmas is well represented by linear theory, and the generated waves play an essential role in the thermodynamics of these systems. The velocity distribution functions (VDFs) characterizing kinetic particle behavior are commonly represented as a sum of anisotropic bi-Maxwellians. A three bi-Maxwellian model is commonly applied for the ions, assuming that the VDF consists of a proton core, a proton beam, and a single He (α) particle population, each with its own density, bulk velocity, and anisotropic temperature. Resolving a secondary α-beam component was generally not possible due to instrumental limitations. The Solar Orbiter Solar Wind Analyser Proton and Alpha Sensor (SWA-PAS) resolves velocity space with sufficient coverage and accuracy to consistently characterize secondary α populations. This design makes the SWA-PAS ideal for examining the effects of α-particle beams on the plasma's kinetic stability. We test the wave signatures observed in the magnetic field power spectrum at ion scales and compare them to the predictions from linear plasma theory, Doppler-shifted into the spacecraft reference frame. We find that taking into account the α-particle beam component is necessary to predict the coherent wave signatures in the observed power spectra, emphasizing the importance of separating the α-particle populations as is traditionally done for protons. Moreover, we demonstrate that the drifts of beam components are responsible for the majority of the modes that propagate in the oblique direction to the magnetic field, while their temperature anisotropies are the primary source of parallel fast magnetosonic modes.

Unified Astronomy Thesaurus concepts: Solar wind (1534); Space plasmas (1544)

1. Introduction

Solar wind plasma is weakly collisional, allowing the medium to depart from local thermodynamic equilibrium (E. Marsch 2012). The particle dynamics are described by a velocity distribution function (VDF), which is commonly approximated as a sum of "component" VDFs, where each component is associated with a particular particle species (e.g., electrons, protons, or helium (α) particles; E. Marsch et al. 1982). In the solar wind, with decades of in situ observations (D. Verscharen et al. 2019), we commonly observe secondary populations within the VDF of a single particle species, typically referred to as beams for ions (B. L. Alterman et al. 2018; R. Bruno et al. 2024) or strahl for electrons (M. Maksimović et al. 2005). Each component, when separated from the core component, has a distinct density n_j and can be anisotropic, with distinct temperatures perpendicular and parallel to the direction of the magnetic field $T_{\perp,j}$, $T_{\parallel,j}$ (L. Matteini et al. 2007), or streaming with different bulk velocities, producing a commonly observed intercomponent drift (T. Ďurovcová et al. 2019). These anisotropies and relative drifts often store a significant percentage of the system's "free" energy (T. K. Fowler 1968; C. H. K. Chen et al. 2016; K. G. Klein et al. 2018; M. M. Martinović & K. G. Klein 2023).

When the amount of free energy exceeds a threshold value, the plasma emits fluctuations in one or more of the system's normal modes, where each emitted mode acts to reduce the free energy source that drives the emission, bringing the system back toward a state of marginal stability. In the case of resonant instabilities, the fluctuations of the electromagnetic field can resonate with a subset of particles, scattering them in velocity space and injecting or removing particle kinetic energy (S. P. Gary 1993; D. Verscharen et al. 2019). The resulting fluctuations are ubiquitous in the solar wind (S. P. Gary et al. 2016; W. Liu et al. 2023) and are commonly observed alongside the out-of-equilibrium VDFs (M. M. Martinović et al. 2021a; A. Afshari et al. 2024). Signatures in the time series of the electric (F. S. Mozer et al. 2021) and magnetic (D. Vech et al. 2021) field, as well as in the power spectra (PS) of both quantities (T. A. Bowen et al. 2020; D. M. Malaspina et al. 2020), provide estimates of wave parameters that can be directly compared to theoretical models. The waves directly resonate with the particles at given resonant velocities (D. Vech et al. 2021; N. Shankarappa et al. 2024), emphasizing their crucial yet not sufficiently explored influence on solar wind evolution.

The interplay of unstable modes and solar wind heating is a central open question to understand the quantitative effects of various solar wind heating mechanisms (L. Matteini et al. 2012). The linear plasma response associated with a VDF is ideally determined by directly integrating functions of the velocity gradients of the phase space density (T. H. Stix 1992; S. P. Gary 1993; D. Verscharen et al. 2018). This calculation is computationally expensive and not suitable for processing mission surveys with millions of observations. Instead, a common approach involves the modeling of the VDF as a known function, e.g., a bi-Maxwellian or κ distribution,

significantly simplifying the integration. For any of these VDF models, the resulting plasma response is a function of a finite number of VDF parameters, e.g., the density, bulk velocity, and temperature anisotropy for each component, referred to as elements of the set $\mathcal{P}$. For a set of VDF parameters, a plethora of available dispersion solvers (K. Roennmark 1982; P. Astfalk et al. 2015; K. G. Klein & G. G. Howes 2015; K. G. Klein et al. 2017; D. Verscharen & B. D. G. Chandran 2018) and machine learning (ML) algorithms (M. M. Martinović & K. G. Klein 2023; V. M. Sadykov et al. 2025) are available to determine the supported normal modes.

The major stumbling block for an accurate description of the waves supported by the plasma is accurate representation of the VDF. In situ particle measurements suffer from inherent limitations in cadence, energy and angular coverage, resolution, and statistical uncertainties (L. B. I. Wilson et al. 2022). Even subtle inaccuracies in the VDF representation lead to notable differences in the results of stability analysis (J. Walters et al. 2023). Another fundamental problem in the treatment of measured VDFs appears in the identification and treatment of secondary components. Ion distributions are most commonly described by single α-particle and single proton Maxwellian components (J. C. Kasper et al. 2006). More sophisticated treatments of the VDF presume the capability of identifying proton beams, where traditionally the largest difficulty is that, in the raw instrument data, the different mass-to-charge ratio of protons and α-particles often cause an overlap between α-particles and drifted proton beams (E. Marsch et al. 1982; J. D. Scudder 2015; B. L. Alterman et al. 2018; T. Ďurovcová et al. 2019). Recent in situ instruments, such as the Solar Probe ANalyzer-Ions on the Parker Solar Probe (PSP; R. Livi et al. 2022) and the Solar Wind Analyser Proton and Alpha Sensor (SWA-PAS; C. J. Owen et al. 2020) on the Solar Orbiter (SolO) provide significantly increased instrument capabilities in accuracy and sampled particle energy-per-charge range, providing the possibility of fitting the secondary α component.

Observations from both Helios (D. Stansby et al. 2019) and Wind (J. C. Kasper et al. 2017) reveal that the temperature ratio between α particles and protons typically peaks around 1 in the slow solar wind, consistent with the expectations for an isothermal fluid. In contrast, this ratio peaks at 4 in the fast solar wind, signaling equal thermal speeds, where heating processes during wind expansion preferentially heat the minority species (E. Marsch & C. Y. Tu 2001; C. Y. Tu & E. Marsch 2001; J. C. Kasper et al. 2008). In some cases, the temperature ratio exceeds 5, indicating the possible involvement of an additional mass proportional heating mechanism (J. C. Kasper et al. 2008). However, while such mechanisms cannot be entirely ruled out, R. Bruno et al. (2024) recently showed that separating the α beam from its core population restores the expected value of 4 when focusing solely on the temperature ratio between the α core and the proton core. These authors suggest that the apparent anomalous increase in α-particle temperatures can instead be attributed to the presence of the relatively massive α beam drifting along the local magnetic field.

Due to the lack of large data sets with reliable separation of the VDF components, statistical evaluations of VDFs with separated α-particle components have not been possible. However, previous studies of the effects of the proton core and beam separation show a fundamental difference in the predicted plasma stability compared to the case with a single proton component. When separating proton beams in observations recorded at 1 au, the number of unstable intervals increases significantly (K. G. Klein et al. 2018). In selected PSP observations, the separation of the beam increases the fraction of unstable intervals from ∼40% to almost 100%, and significantly alters the types of the predicted modes and their propagation directions (K. G. Klein et al. 2021).

In this Letter, we explore the effects of α-particle beams on plasma stability, comparing the inferred unstable modes from VDF parameters obtained by two models: (i) a five-component model—two-proton, two-α, and one-electron plasma; and (ii) a four-component model—two-proton, one-α, and one-electron plasma. The $\mathcal{P}$ sets obtained from the two approaches can fundamentally alter the stability analysis. For example, a moderate, stable drift with respect to the proton core for a one-component α-particle distribution is alternatively represented as a small drift of the α core and potentially unstable drift of the α beam. Additionally, the single α VDF elongated in the parallel direction is separated into two anisotropic VDFs, each with $T_{\perp,j} > T_{\parallel,j}$—resulting in distributions with notably different stability properties. In general, lower secondary α-particle beam drifts and higher anisotropies of the α-particle core induce left-handed (LH) parallel-propagating ion-cyclotron (IC) instabilities (K. G. Klein et al. 2019; M. M. Martinović et al. 2021a). Higher drifts of the secondary proton beam commonly introduce right-handed (RH) fast magnetosonic modes (FMMs; M. M. Martinović & K. G. Klein 2023). Here, we aim to describe the effects of separating the α-particle VDF into two core and beam components, which may be crucial for more accurately characterizing the stability and associated energetic consequences in solar wind plasma.

Observational evidence of relevant wave occurrence arises from comparing modes inferred from the trace PS of the magnetic field, where waves are recognized by a narrowband coherent signal distinct from broadband background turbulence fluctuations. The signature of polarized fluctuations provides confident information about two major parameters: the real part of the wave frequency and wave polarization as measured in the spacecraft frame of reference. Using our stability analysis discussed in the following section and accounting for the Doppler shift from the plasma to the spacecraft frame, we directly compare our dispersion-relation solver results with PS observations. Previous analyses use similar methods to characterize IC heating (T. A. Bowen et al. 2020; N. Shankarappa et al. 2024) and to describe the impacts of α-beams in PSP observations (M. D. McManus et al. 2024). Here, we build on these previous efforts by separating the effects of the two α-particle components, quantifying the differences between the two VDF models and illustrating the importance of carefully distinguishing secondary populations in solar wind plasma.

2. Data Set and Methodology

2.1. Fits of the Velocity Distribution Parameters

SolO SWA-PAS is an electrostatic analyzer with an energy range sufficient to measure protons with velocities up to $\sim$1500 km s^{-1} (C. J. Owen et al. 2020). This range is decreased by a factor of $\sqrt{2}$ for α particles due to the difference in mass-to-charge ratio. SWA-PAS has a standard energy resolution of ∼9.5%, with an 11×9 grid in azimuth and elevation look directions covering a $60^\circ \times 40^\circ$ range,

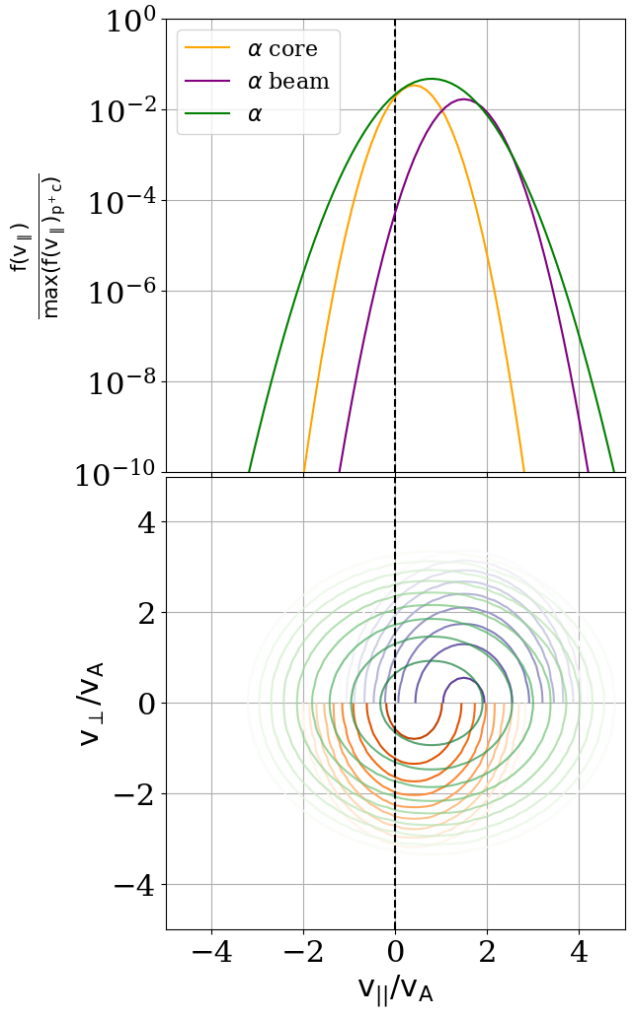

Figure 1. Comparison of the fits of α components for the VDF in parallel sampled by SolO SWA-PAS on 2022 March 2, 16:18:13, using four-component (orange) and five-component (green, purple) models. Parallel cuts at $v_\perp = 0$ and two-dimensional phase space contour maps are given in the top and bottom panels. The extension of the single α-particle component in the parallel direction is evident. The VDFs are centered with respect to the proton core population (not shown), with parameters for both cases listed in Table 1.

ensuring the necessary velocity space coverage to resolve both proton and α secondary populations.

We obtain the distribution parameters for the four- and five-component models using the novel technique detailed in R. De Marco et al. (2023) and R. Bruno et al. (2024) applied directly to the full three-dimensional VDFs collected by SWA-PAS. This approach leverages the clustering analysis technique commonly used in ML to separate the proton core, proton beam, α core, and α beam by identifying subcomponents within the VDF, rather than relying on a conventional bi-Maxwellian fit. Each component of the VDF is given in the form that introduces temperature anisotropies and drifts from the moments of that particular component, which we further treat in an idealized Maxwellian form as

$$f_j(\mathbf{v}) = \frac{n_j}{\pi^{3/2} w_{\perp j}^2 w_{\parallel j}^2} e^{\frac{-v_\perp^2}{w_{\perp j}^2} - \frac{(v_\parallel - \Delta v_\parallel j)^2}{w_{\parallel j}^2}}, \quad (1)$$

where $w_j = \sqrt{2k_b T_j/m_j}$ and k_b is the Boltzmann constant. The differences between the two models are illustrated for a representative interval in Figure 1 and Table 1. Fitting α particles as one or two components renders significant differences in the obtained $\mathcal{P}$ sets and potential sources of free energy.

Table 1
Parameters of the VDFs Shown in Figure 1

$n_\alpha/n_{pc} = 4.8\%$	$n_{\alpha c}/n_{pc} = 3.4\%$	$n_{\alpha b}/n_{pc} = 1.7\%$
$T_{\|\|,pc}/T_{\|\|,\alpha} = 0.11$	$T_{\|\|,pc}/T_{\|\|,\alpha c} = 0.27$	$T_{\|\|,pc}/T_{\|\|,\alpha c} = 0.20$
$T_{\perp,\alpha c}/T_{\|\|,\alpha} = 0.70$	$T_{\perp,\alpha c}/T_{\|\|,\alpha c} = 1.73$	$T_{\perp,\alpha b}/T_{\|\|,\alpha b} = 1.52$
$\Delta v_{\alpha c}/v_A = 0.78$	$\Delta v_{\alpha c}/v_A = 0.40$	$\Delta v_{\alpha b}/v_A = 1.48$

We analyze observations from one representative day, 2022 March 2, when SolO passed through a typical fast solar wind stream at ~0.56 au. The conditions throughout the day are steady and highly Alfvénic with plasma β (i.e., the ratio between thermal and magnetic pressure) of order unity. The observations are available at ~4 s cadence, leading to 14,936 successfully processed intervals for both models, which are used for stability analysis. The quantities of major free energy sources are provided in the top three panels of Figure 2. These panels are clear examples of the common scenario shown in Figure 1—when treated as a single Maxwellian, the drifts of the α particles take values in between the core and beam components from the five-component fits (second panel), while at the same time having artificially increased parallel temperature (third panel). Moreover, the drifts of proton and α beams seem to maintain very similar values. Here, the drifts are normalized to the local Alfvén speed, defined as $v_A = B/\sqrt{\mu_0 n_{pc} m_p}$, where μ_0 is the magnetic permeability of the vacuum and m_p is the proton mass.

2.2. Linear Stability Analysis

Traditional solvers provide solutions to the wave equation for every mode supported by the system, namely those that satisfy $\mathcal{D}(\omega, \boldsymbol{k}, \mathcal{P}) = 0$, where $\mathcal{D}$ is the vector wave equation for a given complex frequency $\omega = \omega_r + i\gamma$, a wavevector $\boldsymbol{k}$, and a set of VDF parameters $\mathcal{P}$. We determine the stability of the VDF with respect to all the ion scale modes by employing the PLUMAGE solver (K. G. Klein et al. 2017), which calculates the Nyquist stability criterion for a hot magnetized collisionless plasma. Over the upper half of the complex frequency plane, the space that contains unstable modes with $\gamma > 0$, the solver performs the contour integral

$$W_n(\boldsymbol{k}, \mathcal{P}) = \frac{1}{2\pi i} \oint \frac{d\omega}{det\,[\mathcal{D}(\omega, \boldsymbol{k}, \mathcal{P})]} \quad (2)$$

to obtain the count of the unstable modes. This integration is repeated by increasing the minimum value of γ until W_n expresses only a single most unstable mode (MUM).

The values of ω and $\boldsymbol{k}$ for a MUM provided by PLUMAGE are then inserted into a PLUME dispersion solver (K. G. Klein & G. G. Howes 2015; K. G. Klein et al. 2025), finding a detailed set of MUM parameters—further on referred to as $\mathcal{W}$—that contains electromagnetic eigenfunctions $\delta\boldsymbol{E}$, $\delta\boldsymbol{B}$, density and velocity fluctuations for each component δn_j and $\delta\boldsymbol{v}_j$, mode polarization σ, and estimated emitted or absorbed power by each component over a wave period P_j. The description of the formalism that calculates the parameter set

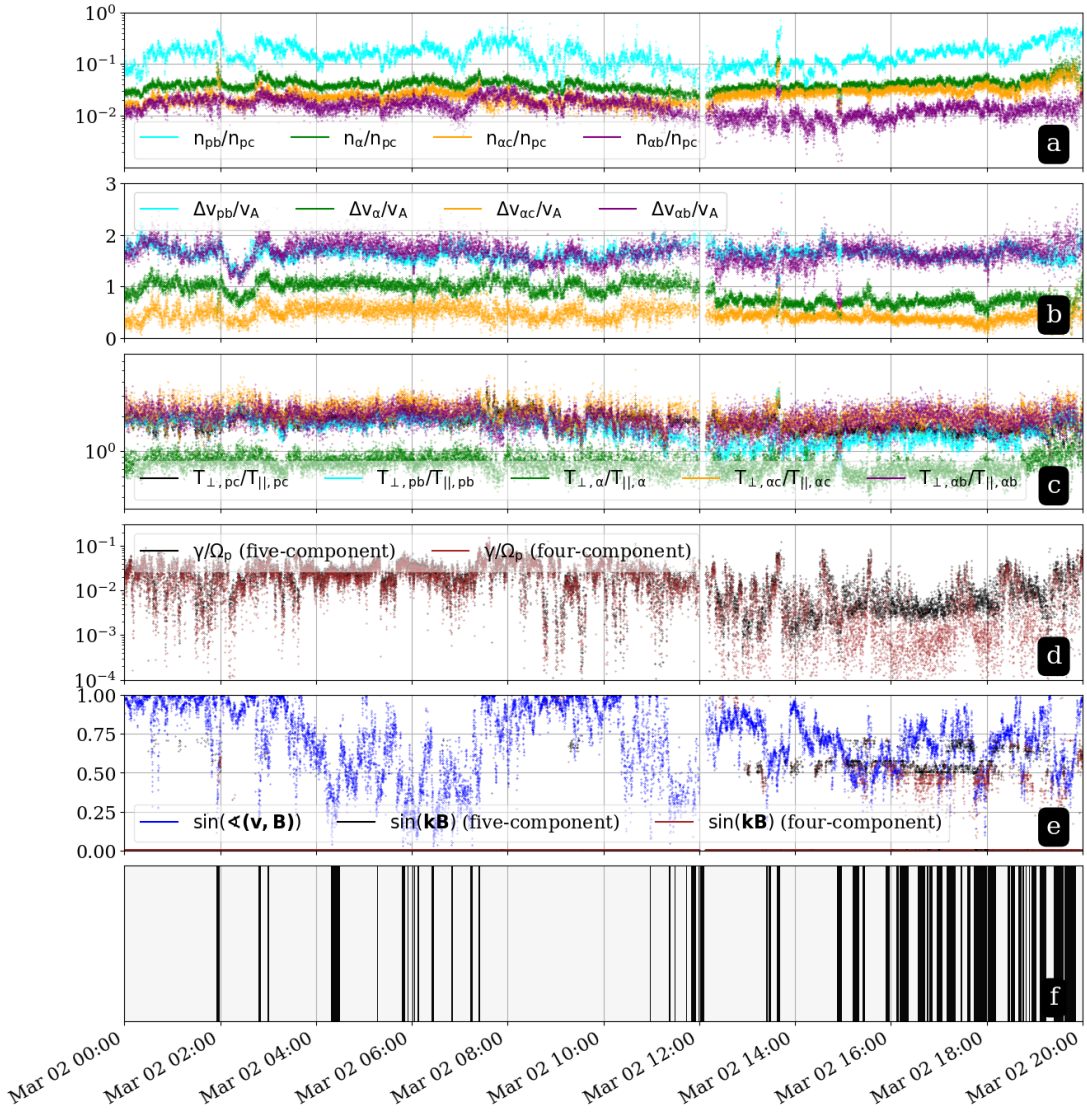

Figure 2. Overview of the VDF parameters used for stability analysis on 2022 March 2. Panels(a)–(c) show the VDF parameters used as input for the stability analysis. Density normalized to n_{pc}, velocity drift normalized to v_A, and temperature anisotropy $T_\perp/T_\parallel$ are shown for the proton core (black), proton beam (cyan), and α particles as a single population (green), α core (brown), and α beam (purple). Panels (d) and (e) show the results of PLUMAGE stability analysis—the normalized growth rates and directions of most unstable modes with respect to the magnetic field and solar wind speed in the spacecraft frame, respectively, for both models. Panel (f) shows the basis for verification of the results, as the intervals where the measured magnetic field polarization in the spacecraft frame marks a clear presence of coherent waves—$\sigma > 0.6$ or $\sigma < -0.6$ (Equation (3))—are marked in black.

$\mathcal{W}$ is given elsewhere (K. G. Klein 2013; R. Huang et al. 2024). Stability analysis that simultaneously uses PLUMAGE and PLUME was previously performed for Wind (K. G. Klein et al. 2018), Helios (K. G. Klein et al. 2019; M. M. Martinović et al. 2021b), and PSP (K. G. Klein et al. 2021; M. D. McManus et al. 2024) observations, with additional technical details described in those references.

Panels (d) and (e) in Figure 2 show the normalized growth rates γ/Ω_p, where $\Omega_p = e_c B/m_p$ is proton cyclotron frequency, and e_c is the elementary charge. Linear Vlasov–Maxwell theory is valid for $\gamma/\omega_r \ll 1$. Since we observe waves with $\omega_r \sim \Omega_p$, the results are comfortably in the domain well described by linear theory. Aside from the time interval 15:00–19:30, most of the unstable modes predicted propagate in the directions parallel or antiparallel to the magnetic field.

2.3. Comparison of Inferred Waves with Observed Power Spectra

The magnetic field vector measurements are provided by the SolO magnetometer (T. S. Horbury et al. 2020) operating in its normal mode, producing eight samples per second. A Morlet wavelet transform (MWT; C. Torrence & G. P. Compo 1998) $\tilde{\boldsymbol{B}}$ combined with minimum variance analysis (MVA; B. U. Ö. Sonnerup & M. Scheible 1998) provides both PS amplitudes and spacecraft frame polarization as functions of time and frequency throughout the day. In contrast to magnetic helicity, polarization σ is defined as the normalized reduced helicity along a single direction as observed by the spacecraft (W. H. Matthaeus & M. L. Goldstein 1982). The MWT for each timescale $s \sim f^{-1}$ and time t is transferred to a coordinate system where the average magnetic field is along the

z-direction, and the minimum variance eigenvector component is along the x-axis. Then, we define σ as

$$\sigma = \frac{2\,\mathrm{Im}[\widetilde{B}_x(s,t)\widetilde{B}_y^*(s,t)]}{|\widetilde{B}_x(s,t)|^2 + |\widetilde{B}_y(s,t)|^2}, \quad (3)$$

where the star stands for complex conjugate. The polarization values provided by MVA are highly variable, and smoothing over time and frequency is required in order to reveal a clear signature of coherent waves on top of the noncoherent background plasma turbulence. The polarization values vary from -1 for RH to $+1$ for LH waves, commonly referred to as electron-resonant and ion-resonant fluctuations (T. A. Bowen et al. 2020; N. Shankarappa et al. 2024). The details of our procedure are given in Appendix B of N. Shankarappa et al. (2024). For direct comparison between the stability analysis and the MVA results, the real frequency values provided by PLUMAGE must be converted into the spacecraft frame of reference. The standard Doppler shift relation $\omega_{sc} = \omega_{plasma} + \boldsymbol{k} \cdot \boldsymbol{v}_{sw(sc)}$ applies, where $\boldsymbol{v}_{sw(sc)}$ is the solar wind speed in the spacecraft frame. The procedure requires careful treatment of variables with respect to inferred wave direction, spacecraft speed, and wave polarization. Details of the calculation for different types of modes are provided by N. Shankarappa et al. (2024). An overview of the results is given in Figure 3.

Direct detection of unstable waves is not always possible due to effects related to the sampling direction. The fluctuations with wavevectors parallel to the velocity vector require lower emitted power in order to be observable in the PS (L. D. Woodham et al. 2021). Also, fluctuations are only detected if their spacecraft frame frequency is lower than the 4 Hz Nyquist frequency of the MWT and if they are continuously emitted for at least several $2\pi\omega_r^{-1}$ periods so that their signature is not removed by our smoothing method. In practice, this set of conditions suggests that mildly unstable modes are difficult to detect due to polarization fluctuations in the background turbulence, while strongly unstable modes—burst-like waves that are emitted over short times—are not detected in the PS due to being smoothed out. Indeed, panels (e) and (f) of Figure 2 show that the clear PS signatures mostly originate from moderately unstable $\sim 10^{-3} \lesssim \gamma/\Omega_p \sim 10^{-2}$ modes.

3. Results and Discussion

3.1. Direct Comparison of Inferred and Measured Instabilities

Our results are summarized in Figure 3. Coloring represents the strongest emitting component—the VDF component with maximum P_j—that drives the MUM for a given interval. PLUMAGE results are matched with the magnetic PS, with solid and hollow circles marking LH and RH polarization, respectively. In the period prior to noon on March 2, the proton core is the strongest emitting component for the vast majority of MUMs. Since the proton core components for both models are largely the same, the inferred modes have very similar properties, and the stream is dominated by LH IC modes (black dots) characteristic of fast, collisionally young solar wind (M. M. Martinović et al. 2021a).

Figure 4 zooms in to three illustrative time windows from Figure 3. In the period between 11:30 and 13:00, the plasma is primarily influenced by the modes created by the proton beam. As the observed RH polarization is less abundant in our data set, we show the details of one of these intervals in Figure 4 (top). The analysis of the dispersion relation of both four-component and five-component VDF models provides the same RH solutions with proton beams as the emitting population.

The importance of a more precise treatment of the α VDF is visible during the second half of the day. Here, four-component analysis predicts the constant presence of the modes induced by the proton beam and the α-particle components in the time period 12:00–19:30. The inferred frequencies in the spacecraft frame for the α-particle induced modes are significantly lower than the ones observed, while the proton-beam-induced modes match with the observed PS in frequency but not in polarization. The example in Figure 4 (middle) shows that these intervals are appropriately addressed by the five-component approach. The observed LH modes are induced by α core anisotropy, which is increased by approximately a factor of 3 for five-component cases due to the separation of the α beam.

A case in which both proton and α core components drive the same mode unstable with the same polarization and frequency is shown in Figure 4 (bottom). Although we cannot distinguish which component of the VDF emits the observed waves from MVA analysis alone, the five-component prediction for α core induced IC waves shows more consistent emission to accompany the strongly polarized observed PS over a wide band of frequencies.

Overall, the stability analysis based on five-component fits shows consistent agreement with the observed PS both in values of observed real frequency and polarization. For the four-component approach, such agreement is observed only for the MUMs driven by the proton core and beam. This is an expected result, as the proton parameters are quantitatively similar for both models.

For the subset of data in which both the four- and five-component models predict unstable modes, in Figure 5, we show the confusion matrix, comparing the statistics of inferred modes (and associated emitting population) between these two models. The values in brackets show the percentages for a subset of 3518 (25%) intervals in which the emitting population is different for the two models. Considering these intervals only, the separation of the α-particle population renders the α-particle core component unstable in almost 40% of cases, primarily due to the increased accuracy of the α-particle core temperature anisotropy (cells (3b–d)). In contrast, removing the artificial increase in $T_{\parallel,\alpha}$ from the four-component model unveils either the proton core or the beam as the carrier of the MUM, as shown in the difference in percentages between cells (1d) and (5c), and between cells (2d) and (5b), respectively. Due to these two factors, the inclusion of the α-particle beams suggests that this component emits the MUM only in $\sim$32% of the five-component intervals (cell (4d)). To further clarify these statistical features, we analyze the physical properties of these modes in Section 3.2. Figure 5 covers only cases in which both models predict unstable VDFs. As the five- and four-component models predict 14,913 (99.8%) and 14,044 (94.2%; cell (5d)) unstable VDFs out of total 14,936, respectively, there is a subset of 846 intervals that are only unstable in the five-component analysis, 692 (82%) of which have the α-particle core as the emitting

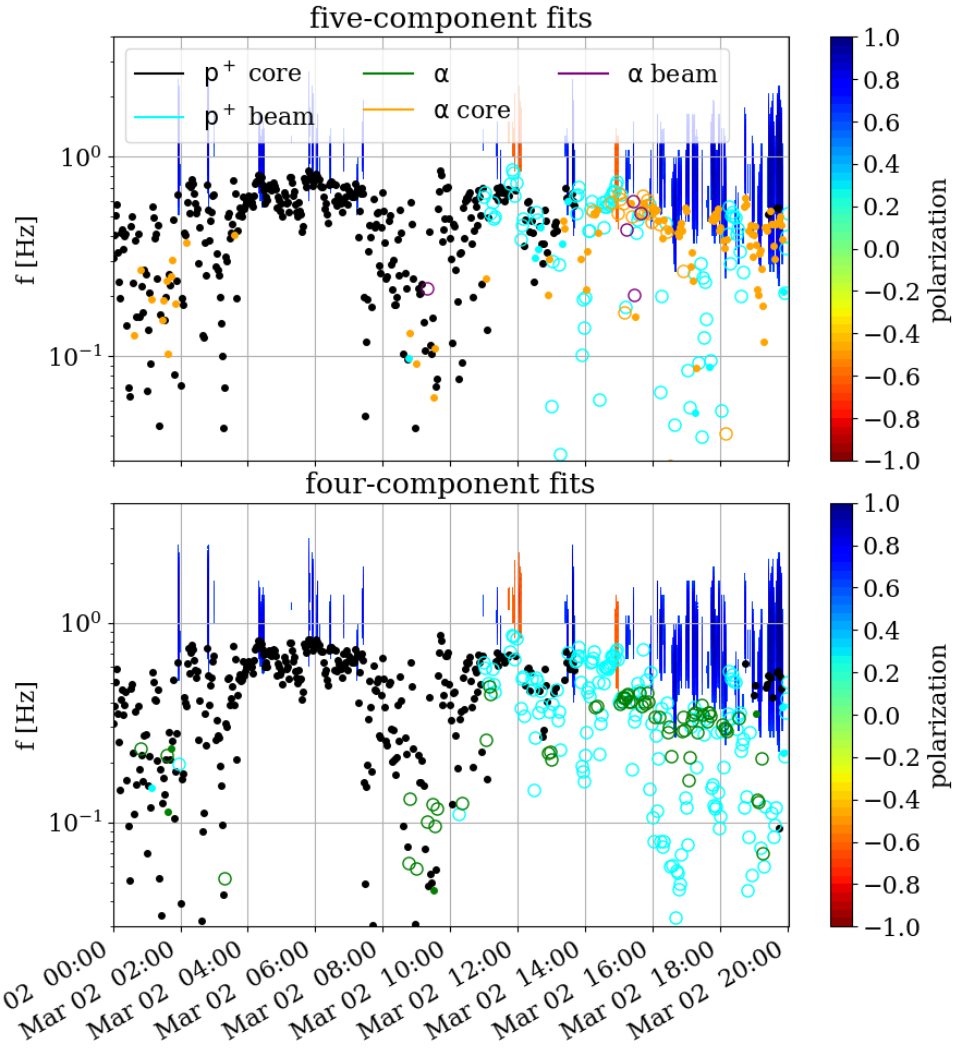

Figure 3. Direct comparison of the frequency and $|\sigma| \geqslant 0.6$ of measured coherent magnetic field fluctuations in the spacecraft frame with the inferred MUM for each interval. LH polarized modes are shown with filled dots and RH with open circle symbols. The color coding of the strongest emitting component for each MUM is the same as in Figure 2. For each emitting component, we show 2 minute median values instead of full cadence for clarity.

component. All 692 intervals predict the LH IC mode induced by temperature anisotropy.

3.2. Analysis of Mode Characteristics

We use the change in polarization σ of MUMs and its propagation direction with respect to the magnetic field to illustrate the behavior of different mode types. After testing all the elements of $\mathcal{P}$ related to the α beam component, we find that the drift $\Delta v_{\alpha b}/v_A$ is the only feature that clearly correlates with $P_{\alpha b}$. Figure 6 (a2) illustrates the increase of the emitted power with increasing drift speed—a relation that cannot be inferred from the four-component treatment. The transition between different types of unstable modes as $\Delta v_{\alpha b}/v_A$ changes is revealed in the direction of propagation switching from parallel to oblique (panel (c2)) and the polarization switching from LH to RH (panel (d2)), while the VDF component inducing the MUM may also change (panel (e2)).

Area I in Figure 6 features MUMs induced by the proton beam (yellow in e2) and the α-particle beam (blue), which lead to wave propagation angle differences (c2) and polarization differences (d2). Strong α-particle beam drift (above $\sim 2v_A$) induces the parallel FMM as the MUM. This is the same mode that becomes unstable for high $\Delta v_{\rm pb}/v_A$ (W. Daughton & S. P. Gary 1998). Although the proton beam drift has similar values to the α drift for the majority of our intervals, the MUM obtained by PLUMAGE analysis is primarily powered by the α drift. These cases require both $\Delta v_{\alpha b}/v_A$ and $T_{\perp,\alpha b} > T_{\parallel,\alpha b}$ to be substantially large and are rare for the heliocentric distances covered by SolO observations. Further exploration via five-component treatment of PSP VDF data is required for further understanding of these modes.

In Area II, as $\Delta v_{\alpha b}/v_A$ decreases, we still find the α beam to be the primary emitting component (e2), but with the drift as the primary source of free energy. Characteristic oblique FMMs appear, acting to decrease the drift, partially dispersing free energy while increasing the α beam anisotropy. This part of parameter space maintains analogy between the behavior of proton and α beams, as similar FMM-induced perpendicular diffusion of protons is predicted in simulations (L. Ofman et al. 2022; L. Pezzini et al. 2024) and through quasi-linear theory (S. M. Shaaban et al. 2024), again leading to conditions for the appearance of parallel FMMs induced by the α beam anisotropy. Proceeding from Area II to III, a specific profile of

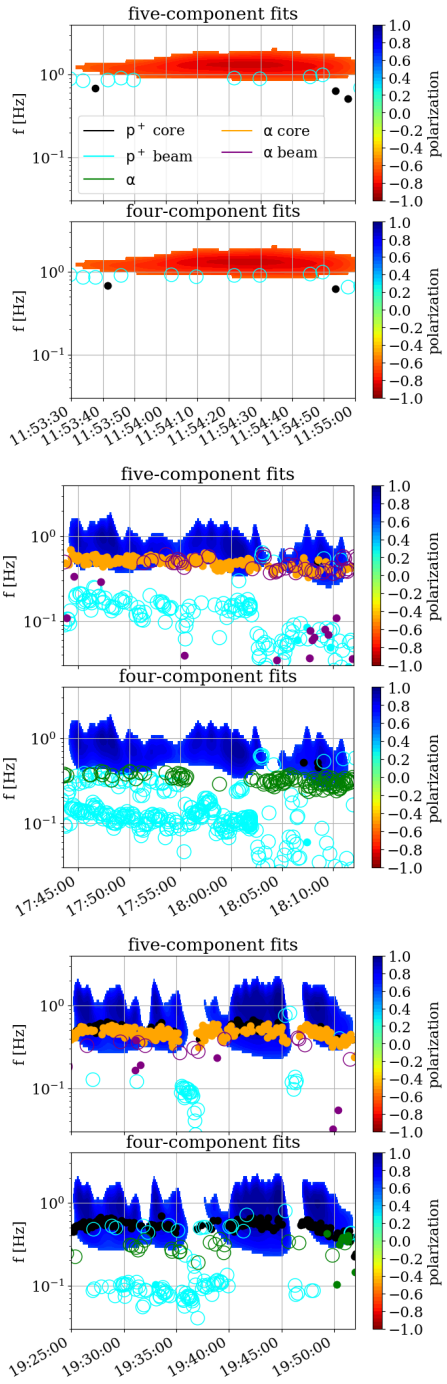

Figure 4. Same as Figure 3, with magnification on specific intervals with full cadence data where RH (top) and LH (bottom) modes are predicted by both models. The middle panel shows the period where the correctly estimated α core temperature anisotropy is necessary for the more accurate description of the observed waves.

$T_{\perp,\alpha b} > T_{\parallel,\alpha b}(\Delta v_{\alpha b}/v_A)$ (b2) shows the temperature anisotropy decreasing as the drift remains on approximately the same level.

Finally, in Area IV, the anisotropy profile rises sharply as the drift is further decreased by the oblique FM. However, the increased $T_{\perp,\alpha b} > T_{\parallel,\alpha b}$ for lower drift emits significantly less power (a2) and is no longer sufficient to be classified as the MUM of the system. The oblique FM, primarily induced by the proton beam drift, becomes the MUM (IV) once the

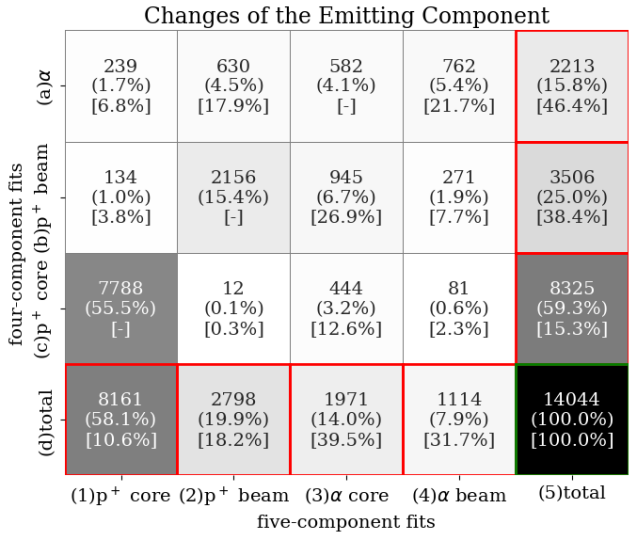

Figure 5. The confusion matrix (CM) of inferred MUMs for four- and five-component models for 14,044 intervals found to be unstable by both models. For each cell, the percentages compared to the total data set population are given in parentheses, while square brackets provide fractions of the nondiagonal part of the CM where different emitting populations are inferred.

$\Delta v_{\alpha b}/v_A$ drift speed is low enough. This "background" mode is often responsible for maintaining the proton beam drift within the confines of marginal linear stability (M. M. Martinović & K. G. Klein 2023). Here, a similar type of oblique FM instability (II) is most likely responsible for limiting the values of $\Delta v_{\alpha b}/v_A$. We emphasize that the two oblique FMMs (II and IV), although induced by similar types of free energy sources, have different effects on the plasma dynamics. Panel (c) of Figure 6 demonstrates that, due to different propagation angles, the two modes can have fundamentally different polarizations. Depending on the combination of $\mathcal{P}$ parameters, most importantly the normalized drift, the unstable modes can be either linearly or circularly polarized.

Figure 7 shows the power emitted by each of the VDF components, polarization, and wavevector of the MUM. Panels (b) and (d) show that parallel-propagating modes induced by secondary components are statistically dominated by RH parallel waves, marked in red. In contrast, core components (a, c) almost exclusively produce parallel LH modes, marked in blue. Oblique modes are induced by proton and α-particle beams, and feature both spherical and linear polarizations, although we do not observe α beam RH oblique modes to be MUMs, probably because these modes appear at lower $\Delta v_{\alpha b}/v_A$ and therefore lower $P_{\alpha b}$ values.

These oblique modes are induced by neither proton nor α-particle core populations. Moreover, Figure 7 illustrates a crucial relation between the polarization of the MUM and its source of free energy. Each panel shows power emitted during a single wave period by a given VDF component, along with the mode polarization. The striking difference in polarization of parallel modes between core and beam population emerges, as core components—from both protons (panel (a)) and α particles (panel (c))—induce LH polarized IC modes, while proton (panel (b)) and α (panel (d)) beam components induce RH polarized FM modes. Oblique instabilities are almost exclusively induced by the beam components. Sorting of the mode polarization and direction of the wavevector has not been observed in previous analyses of the influence of α

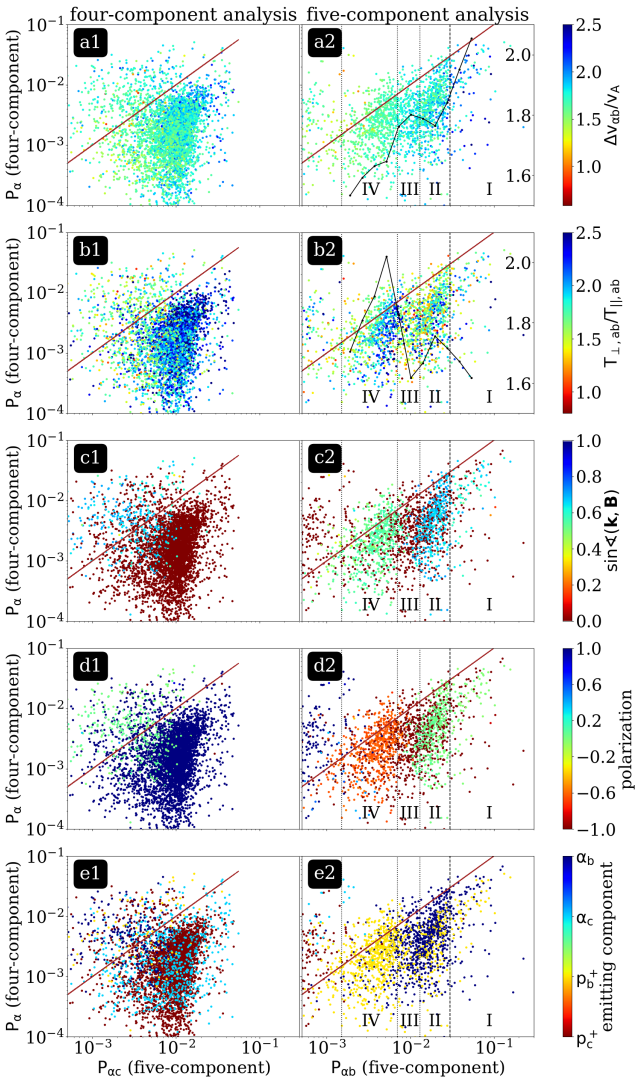

Figure 6. Comparison of the power emitted by a single α component (four-component analysis, column 1) and α core and beams (five-component analysis, column 2), depending on (a1, a2) α beam drift, (b1, b2) α beam temperature anisotropy, (c1, c2) MUM propagation angle, (d1, d2) polarization, and (e1, e2) emitting component. Brown lines mark equal emitting powers. For panels (a1, a2) and (b1, b2), we mark the median values for 12 logarithmically spaced bins with black lines and small dots with labels on the right side. Areas marked with roman numerals are discussed in the text.

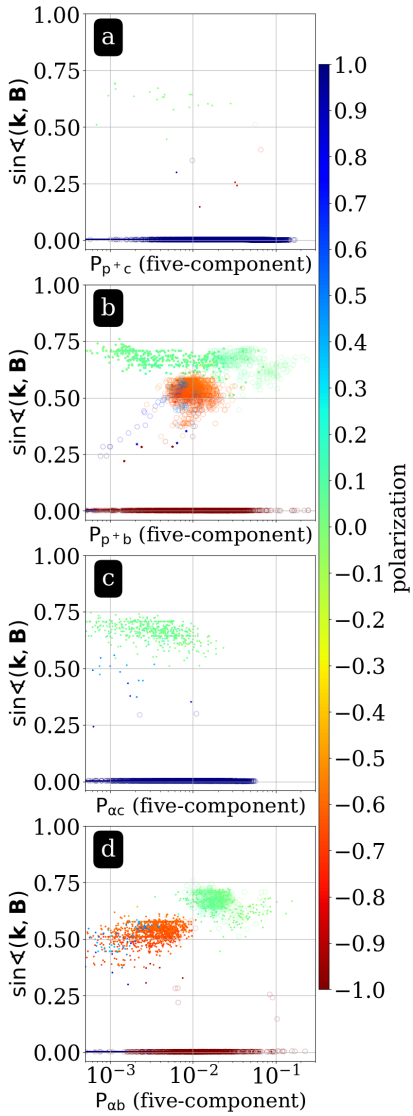

Figure 7. Emitted power over one wave period for each of the VDF components: (a) proton core; (b) proton beam; (c) α-particle core; and (d) α-particle beam. Intervals in which the given component drives the MUM are marked by open circles, while others are shown with filled dots. For easier distinction, all circles are 75% transparent.

particles on linear stability (K. G. Klein et al. 2018; M. M. Martinović & K. G. Klein 2023). We can infer that, for the bulk of observed events, oblique modes are induced by the velocity drifts, while parallel modes are induced by anisotropies.

Our division of power emission into components neglects the effects of the energy exchange between all of the components at the resonant velocities specific to a given mode's frequency ω_r and wavevector k. These interactions can lead to one or more components partially absorbing the power emitted by another component, leading to subtle changes in the growth rate and eigenfunction values. It would be worthwhile to investigate the intricacies of these particle–mode resonances in future work.

These results have a profound consequence for our understanding of in situ heating of α particles. Remote sensing observations of the corona suggest that the plasma is highly anisotropic in the perpendicular direction ($T_\perp > T_\parallel$) for both protons and α particles (S. R. Cranmer 2002). However, the in situ data sampled by Helios at 0.3–0.7 au and processed in mission surveys (D. Stansby et al. 2018; T. Ďurovcová et al. 2019) clearly suggest the opposite ($T_{\perp,\alpha} < T_{\parallel,\alpha}$), with notable, and sometimes extreme, elongations of the α population in the parallel direction. Although several mechanisms, such as Landau damping (N. Shankarappa et al. 2023), transit time damping (R. Huang et al. 2024), or magnetic pumping (E. Lichko et al. 2017; E. Lichko & J. Egedal 2020; P. Montag & G. G. Howes 2022), preferably heat particles in the direction parallel to the magnetic field, none of them are expected to be highly effective toward α particles without simultaneously affecting protons in the same fashion (S. R. Cranmer & A. A. van Ballegooijen 2012). On the contrary, it is well established that the processes that preferably heat the plasma in the perpendicular direction, such as IC heating (T. A. Bowen et al. 2020, 2024; A. Afshari et al.

2024) and stochastic heating (B. D. G. Chandran et al. 2010; M. M. Martinović et al. 2020), are not just measured throughout the inner heliosphere but are also more prominent at lower radial distances (M. M. Martinović et al. 2019; W. Liu et al. 2023).

4. Conclusions

Our results highlight the importance of accounting for the secondary α-particle VDF component for the more accurate identification of linearly unstable modes and the free energy sources driving them. If the α particles are treated as one bi-Maxwellian instead of a more accurate representation with two bi-Maxwellians, the two significant parameters for both core and beam—relative drift and temperature anisotropy—may be significantly altered. As demonstrated in this work, the MUMs inferred only by the five-component treatment do not necessarily originate from the α-particle beams, but also from the α-particle core, as the five-component treatment enables a correct evaluation of its anisotropy.

The results presented here can be summarized by two important points. In general, (1) while parallel-propagating modes are primarily induced by anisotropies, oblique modes are primarily induced by drifts; and (2) core populations are primarily responsible for parallel LH IC modes, while beams' temperature anisotropies are primarily responsible for parallel RH FMMs. Although these rules have exceptions that we will elaborate in detail in future work, this simplified model provides a useful description of the underlying solar wind stability dynamics given the complexity of the observed plasma equilibrium.

The behavior of MUMs induced by proton and α-particle beams shows striking similarities. Neglecting both the proton beams (K. G. Klein et al. 2021) and α beams from the linear stability analysis removes the prediction of oblique modes and RH FMMs that are clearly observed in the magnetic field PS. Also, both components feature an oblique FM at lower drifts, which is responsible for maintaining similar drift values and trends for the two components.

The implications of the difference in treatment of the VDF are wider than just changes of the inferred instabilities. Depending on whether the four-component or the five-component model is used, the different mode types propagate with different wavelengths, consequently interacting with different parts of the VDF (D. Verscharen et al. 2019). This process is significantly faster than collisional relaxation, and thus the signatures of wave–particle interaction on the VDF determine the ability of particles to subsequently emit or absorb additional waves. Therefore, the difference in the treatment of α particles has rippling consequences for our understanding of energy transport and dissipation in the solar wind. This is the case primarily for the regions of the solar wind where α-particle density is high, such as ICMEs I. G. Richardson & H. V. Cane (2004), streamer belts (J. Huang et al. 2023), and coronal hole fast solar wind (E. Marsch et al. 1982; J. C. Kasper et al. 2006).

Acknowledgments

Solar Orbiter is a space mission of international collaboration between ESA and NASA, operated by ESA. Solar Orbiter SWA data are derived from scientific sensors that have been designed and created, and are operated under, funding provided in numerous contracts from the UK Space Agency (UKSA), the UK Science and Technology Facilities Council (STFC), the Agenzia Spaziale Italiana (ASI), the Centre National d'Études Spatiales (CNES, France), the Centre National de la Recherche Scientifique (CNRS, France), the Czech contribution to the ESA PRODEX program, and NASA. The Italian contribution to Solar Orbiter SWA at INAF/IAPS is currently funded under ASI grant 2018-30-HH.1-2022. Special thanks are extended to IRAP/CNRS for SWA-PAS operations and data calibration, and to the MAG team for providing Solar Orbiter magnetic field data. M.M.M. and K.G. K. were financially supported by NASA grants: 80NSSC22K1011, 80NSSC19K1390, 80NSSC23K0693, 80NSSC19K0829, and 80NSSC24K0724. An allocation of computer time from the UA Research Computing High Performance Computing at the University of Arizona is gratefully acknowledged. D.V. is supported by STFC Consolidated grant ST/W001004/1. R.D.M. is supported by the INAF 2023 Fundamental Research grant "Machine Learning on Solar Wind Velocity Distribution Functions." This research was supported by the International Space Science Institute (ISSI) in Bern, through ISSI International Team project #563 (Ion Kinetic Instabilities in the Solar Wind in Light of Parker Solar Probe and Solar Orbiter Observations) led by L. Ofman and L. Jian.

ORCID iDs

Mihailo M. Martinović https://orcid.org/0000-0002-7365-0472
Kristopher G. Klein https://orcid.org/0000-0001-6038-1923
Rossana De Marco https://orcid.org/0000-0002-7426-7379
Daniel Verscharen https://orcid.org/0000-0002-0497-1096
Roberto Bruno https://orcid.org/0000-0002-2152-0115
Raffaella D'Amicis https://orcid.org/0000-0003-2647-117X

References

Afshari, A., Howes, G., Shuster, J., et al. 2024, NatCo, 15, 7870
Alterman, B. L., Kasper, J. C., Stevens, M. L., & Koval, A. 2018, ApJ, 864, 112
Astfalk, P., Görler, T., & Jenko, F. 2015, JGRA, 120, 7107
Bowen, T. A., Mallet, A., Huang, J., et al. 2020, ApJS, 246, 66
Bowen, T. A., Vasko, I. Y., Bale, S. D., et al. 2024, ApJL, 972, L8
Bruno, R., De Marco, R., D'Amicis, R., et al. 2024, ApJ, 969, 106
Chandran, B. D. G., Li, B., Rogers, B. N., Quataert, E., & Germaschewski, K. 2010, ApJ, 720, 503
Chen, C. H. K., Matteini, L., Schekochihin, A. A., et al. 2016, ApJL, 825, L26
Cranmer, S. R. 2002, SSRv, 101, 229
Cranmer, S. R., & van Ballegooijen, A. A. 2012, ApJ, 754, 92
Daughton, W., & Gary, S. P. 1998, JGR, 103, 20613
De Marco, R., Bruno, R., Jagarlamudi, V. K., et al. 2023, A&A, 669, A108
Ďurovcová, T., Šafránková, J., & Němeček, Z. 2019, SoPh, 294, 97
Fowler, T. K. 1968, AdPlP, 1, 201
Gary, S. P. 1993, Theory of Space Plasma Microinstabilities (Cambridge: Cambridge Univ. Press)
Gary, S. P., Jian, L. K., Broiles, T. W., et al. 2016, JGRA, 121, 30
Horbury, T. S., O'Brien, H., Carrasco Blazquez, I., et al. 2020, A&A, 642, A9
Huang, J., Kasper, J. C., Fisk, L. A., et al. 2023, ApJ, 952, 33
Huang, R., Howes, G. G., & McCubbin, A. J. 2024, JPlPh, 90, 535900401
Kasper, J. C., Klein, K. G., Weber, T., et al. 2017, ApJ, 849, 126
Kasper, J. C., Lazarus, A. J., & Gary, S. P. 2008, PhRvL, 101, 261103
Kasper, J. C., Lazarus, A. J., Steinberg, J. T., Ogilvie, K. W., & Szabo, A. 2006, JGRA, 111, A03105
Klein, K. G. 2013, PhD thesis, Univ. Iowa

Klein, K. G., Alterman, B. L., Stevens, M. L., Vech, D., & Kasper, J. C. 2018, PhRvL, 120, 205102
Klein, K. G., & Howes, G. G. 2015, PhPl, 22, 032903
Klein, K. G., Howes, G. G., & Brown, C. R. 2025, RNAAS, 9, 102
Klein, K. G., Kasper, J. C., Korreck, K. E., & Stevens, M. L. 2017, JGRA, 122, 9815
Klein, K. G., Martinović, M., Stansby, D., & Horbury, T. S. 2019, ApJ, 887, 234
Klein, K. G., Verniero, J. L., Alterman, B., et al. 2021, ApJ, 909, 7
Lichko, E., & Egedal, J. 2020, NatCo, 11, 2942
Lichko, E., Egedal, J., Daughton, W., & Kasper, J. 2017, ApJL, 850, L28
Liu, W., Zhao, J., Wang, T., et al. 2023, ApJ, 951, 69
Livi, R., Larson, D. E., Kasper, J. C., et al. 2022, ApJ, 938, 138
Maksimović, M., Zouganelis, Y., Chaufray, J. Y., et al. 2005, JGRA, 110, A09104
Malaspina, D. M., Halekas, J., Berčič, L., et al. 2020, ApJS, 246, 21
Marsch, E. 2012, SSRv, 172, 23
Marsch, E., Schwenn, R., Rosenbauer, H., et al. 1982, JGRA, 87, 52
Marsch, E., & Tu, C. Y. 2001, JGRA, 106, 8357
Martinović, M. M., & Klein, K. G. 2023, ApJ, 952, 14
Martinović, M. M., Klein, K. G., & Bourouaine, S. 2019, ApJ, 879, 43
Martinović, M. M., Klein, K. G., Ďurovcová, T., & Alterman, B. L. 2021a, ApJ, 923, 116
Martinović, M. M., Klein, K. G., Huang, J., et al. 2021b, ApJ, 912, 28
Martinović, M. M., Klein, K. G., Kasper, J. C., et al. 2020, ApJS, 246, 30
Matteini, L., Hellinger, P., Landi, S., Trávníček, P. M., & Velli, M. 2012, SSRv, 172, 373
Matteini, L., Landi, S., Hellinger, P., et al. 2007, GeoRL, 34, L20105
Matthaeus, W. H., & Goldstein, M. L. 1982, JGR, 87, 6011
McManus, M. D., Klein, K. G., Bale, S. D., et al. 2024, ApJ, 961, 142
Montag, P., & Howes, G. G. 2022, PhPl, 29, 032901
Mozer, F. S., Vasko, I. Y., & Verniero, J. L. 2021, ApJL, 919, L2
Ofman, L., Boardsen, S. A., Jian, L. K., Verniero, J. L., & Larson, D. 2022, ApJ, 926, 185
Owen, C. J., Bruno, R., Livi, S., et al. 2020, A&A, 642, A16
Pezzini, L., Zhukov, A. N., Bacchini, F., et al. 2024, ApJ, 975, 37
Richardson, I. G., & Cane, H. V. 2004, JGRA, 109, A09104
Roennmark, K. 1982, Waves in Homogeneous, Anisotropic Multicomponent Plasmas (WHAMP) KGI Rep. No. 179, Kiruna Geophysical Institute
Sadykov, V. M., Ofman, L., Boardsen, S. A., et al. 2025, ApJ, 279, 28
Scudder, J. D. 2015, ApJ, 809, 126
Shaaban, S. M., Lazar, M., López, R. A., Yoon, P. H., & Poedts, S. 2024, A&A, 692, L6
Shankarappa, N., Klein, K. G., & Martinović, M. M. 2023, AJ, 946, 85
Shankarappa, N., Klein, K. G., Martinović, M. M., & Bowen, T. 2024, ApJ, 973, 20
Sonnerup, B. U. Ö., & Scheible, M. 1998, ISSIR, 1, 185
Stansby, D., Perrone, D., Matteini, L., Horbury, T. S., & Salem, C. S. 2019, A&A, 623, L2
Stansby, D., Salem, C., Matteini, L., & Horbury, T. 2018, SoPh, 293, 155
Stix, T. H. 1992, Waves in Plasmas (Berlin: Springer)
Torrence, C., & Compo, G. P. 1998, BAMS, 79, 61
Tu, C. Y., & Marsch, E. 2001, JGR, 106, 8233
Vech, D., Martinović, M. M., Klein, K. G., et al. 2021, A&A, 650, A10
Verscharen, D., & Chandran, B. D. G. 2018, RNAAS, 2, 13
Verscharen, D., Klein, K. G., Chandran, B. D. G., et al. 2018, JPlPh, 84, 905840403
Verscharen, D., Klein, K. G., & Maruca, B. A. 2019, LRSP, 16, 5
Walters, J., Klein, K. G., Lichko, E., et al. 2023, ApJ, 955, 97
Wilson, L. B. I., Goodrich, K. A., Turner, D. L., et al. 2022, FrASS, 9, 369
Woodham, L. D., Wicks, R. T., Verscharen, D., TenBarge, J. M., & Howes, G. G. 2021, ApJ, 912, 101